

Disentangling the Impact of Quasiparticles and Two-Level Systems on the Statistics of Superconducting Qubit Lifetime

Shaojiang Zhu,^{1,*} Xinyuan You,¹ Ugur Alyanak,^{1,2} Mustafa Bal,¹ Francesco Crisa,¹ Sabrina Garattoni,¹ Andrei Lunin,¹ Roman Pilipenko,¹ Akshay Murthy,¹ Alexander Romanenko,¹ and Anna Grassellino¹

¹*Superconducting Quantum Materials and Systems Center,*

Fermi National Accelerator Laboratory, Batavia, IL 60510, USA

²*Department of Physics, University of Chicago, Chicago, IL 60637, USA*

Temporal fluctuations in the superconducting qubit lifetime, T_1 , bring up additional challenges in building a fault-tolerant quantum computer. While the exact mechanisms remain unclear, T_1 fluctuations are generally attributed to the strong coupling between the qubit and a few near-resonant two-level systems (TLSs) that can exchange energy with an assemble of thermally fluctuating two-level fluctuators (TLFs) at low frequencies. Here, we report T_1 measurements on the qubits with different geometrical footprints and surface dielectrics as a function of the temperature. By analyzing the noise spectrum of the qubit depolarization rate, $\Gamma_1 = 1/T_1$, we can disentangle the impact of TLSs, non-equilibrium quasiparticles (QPs), and equilibrium (thermally excited) QPs on the variance in Γ_1 . We find that Γ_1 variances in the qubit with a small footprint are more susceptible to the QP and TLS fluctuations than those in the large-footprint qubits. Furthermore, the QP-induced variances in all qubits are consistent with the theoretical framework of QP diffusion and fluctuation. We suggest these findings can offer valuable insights for future qubit design and engineering optimization.

Superconducting qubits are a promising candidate for building a fault-tolerant quantum computer with their flexibility in circuit design [1–5]. This progress has been significantly propelled by the enhancement of qubit lifetime, T_1 , from the nanosecond to millisecond range over the past decades, advanced by improvements in material science, nanofabrication technology, and microwave design and engineering [6–8]. Meanwhile, it has been observed in experiments that the qubit T_1 , as well as the decoherence time T_2 and qubit frequency, can fluctuate across the time and frequency domains; the qubits with higher T_1 show larger fluctuations [9–13]. Since currently the gate fidelity is primarily limited by qubit coherence, this fluctuation introduces additional challenges and obstacles to quantum error correction and future scalability.

Although the underlying physics are not yet fully understood, two-level defects residing in the amorphous dielectrics at the material surfaces are suggested as the major decoherence source in superconducting quantum devices [13–16]. High-frequency, near-resonance TLSs strongly couple to the qubit and dissipate energy to the ambient environment, causing qubit depolarization. Recently, Müller *et al.* pointed out that high-frequency TLSs can also interact with thermally fluctuating TLFs at frequencies below the environment temperature via dipole-dipole interactions. This can result in the fluctuation of qubit T_1 [9]. Subsequent experimental studies of both flux-tunable and fixed-frequency transmon qubits support this theory by showing the signatures of a few TLSs responsible for the qubit lifetime fluctuation. Specifically, the spectral density of the qubit lifetime extracted from measurements exhibits both Lorentzian and $1/f$ type behavior [10, 11, 17].

Since the number of QPs can fluctuate due to mechanisms such as generation and recombination [18], it is natural to hypothesize that these same mechanisms can lead to fluctuations in the coherence of superconducting qubits. To eluci-

date the observed power law relationship between the average and standard deviation of qubit T_1 , an assumption that the qubit T_1 is only limited by the population of thermally excited QPs was made for this purpose [19, 20]. The same assumption was used to explain temporal fluctuations of qubit T_1 extracted from the double exponential decay in the relaxations curves [21]. By examining the T_1 fluctuations at a few selected temperatures, Müller *et al.* briefly discussed the contributions of both TLSs and QPs on the T_1 fluctuations in the same qubit and suggested that, if there is any, the fluctuation due to QPs is likely to be smaller than the one associated with strongly coupled TLSs [9].

While many studies have focused on understanding qubit T_1 fluctuations induced by either TLSs or QPs, it is practically interesting to investigate both impacts in the same device and disentangle each fluctuation source to understand the decoherence mechanisms better and propose strategies to mitigate these noise channels. In this work, we perform T_1 measurements on three fixed-frequency transmon qubits with different geometrical footprints and surface dielectrics over a temperature range of 7-153 mK. Continuous T_1 measurements of ~ 72 hours at each temperature allow us to analyze the spectral density of qubit fluctuations in terms of depolarization rate, Γ_1 , across a broad range of frequencies, from which we can extract the contributions of the TLSs and QPs to the variance in Γ_1 . We find that the qubit with a small footprint is more sensitive to the QP and TLS fluctuations. We further analyze the QP densities near the qubit junction based on a diffusion model and provide quantitative support on the experimental observations of qubit Γ_1 variances induced by non-equilibrium and equilibrium QPs, respectively.

We label the three qubits under study as A, B, and C, all of which are fabricated on two separate but identical Sapphire wafers (A and B are on one wafer and C on another). Both wafers share the same qubit layout, and each qubit has its own $\lambda/4$ coplanar waveguide resonator that is inductively coupled

to a common feedline for qubit dispersive readout. Qubits A and B use a 160 nm Nb thin film for the patterned capacitor pads, while qubit C uses the same thick Nb film with *in situ* encapsulated ~ 10 nm Ta on the top. Qubit A has small pads ($120 \times 510 \mu\text{m}^2$) separated by a $20 \mu\text{m}$ gap, and qubits B and C adopt the same geometry, specifically, $150 \times 720 \mu\text{m}^2$ pads with a $150 \mu\text{m}$ gap. The fabrication processes are kept nominally identical for the two wafers, and the same size of Al/AIO_x/Al junction is used for all the qubits. The two chips are packaged in the same type of enclosures (Cu coated with Au), wired on two separate measurement chains that have nominally identical configurations, and characterized in the same cooldown. Additional details regarding the qubit fabrication, material characterization, and microwave measurements can be found in Ref. 12. In terms of TLS losses, our microwave simulation based on the full 3D model shows that the energy participation ratio (EPR) of the surface dielectric in qubit A is about two times larger than that in qubits B and C (see details in Supplementary Material). The dielectric losses of the surface oxide on metal pads of qubits A and B are the same, reported to be on the order of $\delta_{\text{NbO}_x} \sim 10^{-2}$ [22, 23]; the dielectric loss $\delta_{\text{TaO}_x} \sim 10^{-3}$ [24] of qubit C is about an order of magnitude lower than that of qubits A and B.

At each elevated temperature, we wait for two hours to thermalize the qubits, before performing qubit T_1 measurements consecutively for about 72 hours. Qubits A and B measurements are interleaved, while qubit C's are continuous. Each T_1 decay curve takes about 6 to 13 minutes, depending on the T_1 value of the qubits. In the following analyses, we assume that the TLSs and QPs primarily determine the depolarization rate of our qubits due to the following facts: (1) the Purcell rate of the qubit is experimentally verified to be below 1 kHz, (2) the loss due to trapped flux in the pads is negligible because all qubits are fixed-frequency transmons with a single, sub-micron Josephson junction, and (3) the enclosure is designed to have the lowest resonance mode at 10 GHz, well above the qubit frequency (approximately 4 GHz). Therefore, we can write the qubit depolarization rate as the sum of the TLS and QP losses, *i.e.*, $\Gamma_1 = \Gamma_{\text{TLS}} + \Gamma_{\text{QP}}$, with $\Gamma_{\text{TLS}} = p\delta_{\text{TLS}}$. Here p is the geometry-dependent EPR and δ_{TLS} is determined by the surface dielectric of the metal pads. In this work, we only consider the dielectric loss from the metal-air interface [12].

Figure 1(a) shows the temporal Γ_1 fluctuations of qubit B at 7 mK (blue) and 153 mK (red), respectively. At low temperatures, the Γ_1 fluctuation resembles telegraphic noise, characterized by instantaneous switching and finite dwell time, which is a signature of the TLS-TLF interaction [9, 17]. At higher temperatures, the Γ_1 fluctuation shows white noise behavior, consistent with the behavior due to fluctuations in the QP number [18]. To disentangle the contributions of TLSs and QPs to the Γ_1 fluctuations, we convert the temporal fluctuations to spectral density by performing the Fourier transform of the autocorrelation function of the qubit depolarization rate $\langle \Gamma_1(t)\Gamma_1(0) \rangle$, following the method reported in Ref. 9. The obtained spectral densities of qubit B at 7 mK (blue dot) and 153 mK (red dot) are shown in Fig. 1(b) as a function of fre-

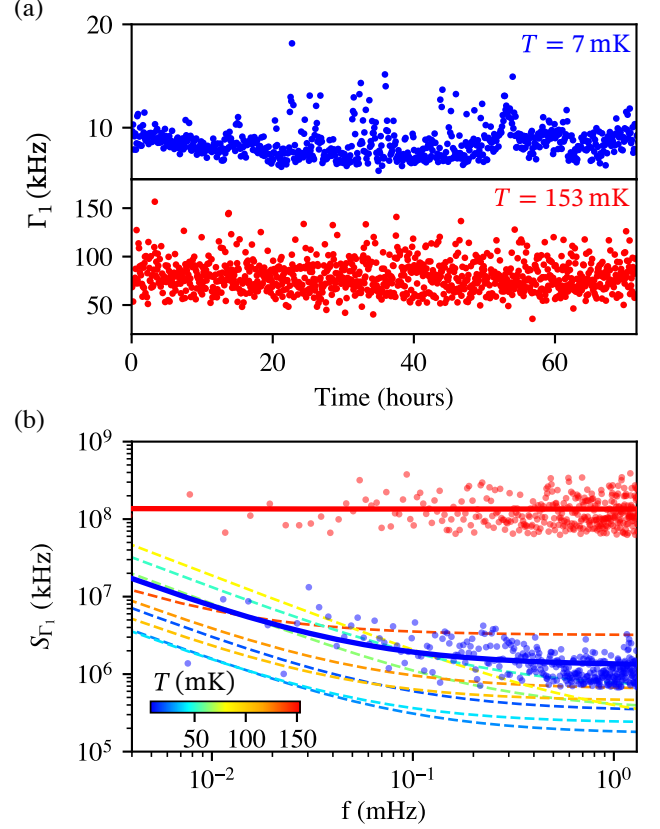


FIG. 1. (a) Typical Γ_1 temporal fluctuations of qubit B at 7 mK (blue) and 153 mK (red), respectively. At low temperatures, typical telegraphic noise of Γ_1 fluctuations with instantaneous switching and finite dwell time exhibits signatures of the TLS-TLF interaction. At high temperatures, the white noise behavior of Γ_1 indicates that the QP fluctuations are the dominating noise source. (b) The noise spectrum of qubit depolarization rate S_{Γ_1} at 7 mK and 153 mK are plotted as the solid symbols. The two data sets are fitted with equation $S_{\Gamma_1}(f) = a/f + b$ and shown as the solid lines. The dashed lines are the fitted curves at all other temperatures, illustrating the transition of the dominating noise source from TLSs at low temperatures to QPs at high temperatures.

quency. At low temperature ($T = 7$ mK), we observe a clear $1/f$ behavior at low frequency and a white noise behavior at high frequency. The former behavior is predicted within the interacting TLS-TLF model, where a few TLSs undergo frequency fluctuations due to interactions with an assembly of thermal TLFs [9]. On the other hand, it is known that the number of QPs can fluctuate due to the dynamics of QP generation and recombination. This results in a Lorentzian-type spectral density [18, 25]. Since the frequencies we measured here are much smaller than the characteristic QP recombination rate (\sim kHz), the Lorentzian profile can be well approximated as constant white noise. Therefore, we fit the data with the equation $S_{\Gamma_1}(f) = a/f + b$, with results shown as thick solid lines in Fig. 1(b). At higher temperature ($T = 153$ mK), the spectral density mostly exhibits white noise behavior, indicating that QPs dominate the fluctuation. In Fig. 1(b), we

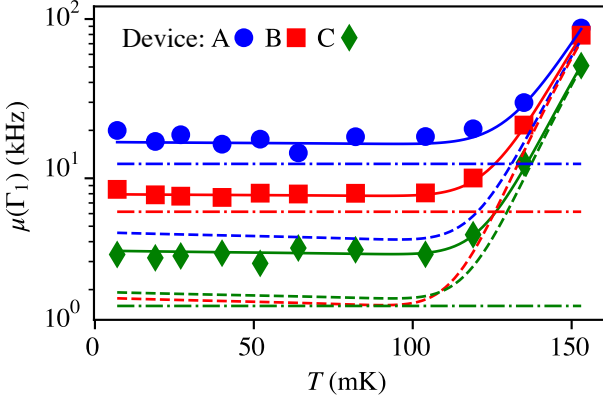


FIG. 2. Temperature dependence of the average depolarization rate $\mu(\Gamma_1)$ for all three qubits. Solid symbols represent the data, dash-dotted lines are the fitted contribution from TLS, and dashed lines are the fitted contribution from both non-equilibrium and equilibrium QPs. Solid lines show the sum of the TLS and QP losses, which is in agreement with the measured data. The extracted fitting parameters are provided in Table I.

also plot the fitted curves at different temperatures to illustrate the transition of dominating noise source from TLSs at low temperatures to QPs at high temperatures.

We next analyze the impact of QP and TLS losses on the qubit average Γ_1 , $\mu(\Gamma_1)$, as a function of temperature. The measurement data is shown as solid symbols in Fig. 2. It is seen that $\mu(\Gamma_1)$ of all three qubits show weak temperature dependence when temperatures are below ~ 100 mK, then exponentially increase and approach the same value around 153 mK. Based on established TLS and QP theories, we can disentangle the TLS and QP loss contributions to the $\mu(\Gamma_1)$. First, although both the relaxation and excitation rate of the qubit due to a single TLS depend on temperature, the sum of both, *i.e.*, the total TLS depolarization rate contributing to the qubit is temperature independent [26, 27]. Secondly, the contributions of QPs to the qubit Γ_1 can be written as [18, 28]:

$$\Gamma_{qp} = \frac{16E_J}{\hbar\pi} \sqrt{\frac{E_C}{8E_J}} \sqrt{\frac{2\Delta}{\pi k_B T}} \exp\left(\frac{\hbar\omega_q}{2k_B T}\right) K_0\left(\frac{\hbar\omega_q}{2k_B T}\right) x_{qp}, \quad (1)$$

where E_J and E_C are the Josephson and charging energies of the qubit with transition frequency ω_q . $K_0(z)$ is a modified Bessel function. x_{qp} is defined as the QP number density $n_{qp} = N_{qp}/V$ normalized by the Cooper pair number density $n_{cp} = 2\nu_0\Delta$, with $\nu_0 \approx 1(\text{eV}\text{\AA}^3)^{-1}$ [29]. The temperature dependence of x_{qp} is modeled as $x_{qp} = x_{qp}^0 + \sqrt{2\pi k_B T/\Delta} \exp(-\Delta/k_B T)$, where the first term describes the non-equilibrium QP density that is temperature independent, and the second term denotes the equilibrium (thermal) QP density that is exponentially dependent on the temperature. Using the experimentally determined E_J , E_C , and ω_q , we can fit the data to extract the TLS loss rate Γ_{TLS} , non-equilibrium QP density x_{qp}^0 , and superconducting gap Δ . Fit-

ted results are shown in Table I [30].

From the fits, all three qubits show similar gap energy $\Delta/2\pi \sim 40$ GHz, which is compatible with the values reported in the literature [31, 32], although slightly lower. This is likely due to differences in Al film thicknesses and fabrication processes. The extracted Γ_{TLS} values are shown as dash-dotted lines in Fig. 2, and the improvement of Γ_{TLS} from qubit A to C can be explained by either the simulated EPR or the differences in dielectric loss. The ratio of Γ_{TLS} between qubit A and B is about 1.9, which matches our EPR simulation; the ratio between qubit B and C is about 3.9, smaller than the reported $\delta_{\text{NbO}_x}/\delta_{\text{TaO}_x} \sim 10$ [22–24]. This discrepancy might arise because in qubit C the Ta thin film only encapsulates the Nb top surface but not the sidewall [12]. The contribution from QPs is shown as dashed lines in Fig. 2. As expected, Γ_{qp} is dominated by the equilibrium (thermal) QP density x_{qp}^{th} at temperatures, $k_B T$, above the Al gap, Δ , and by the non-equilibrium QP density x_{qp}^0 when $k_B T$ is below Δ . However, it is noteworthy that, although the junctions in all three qubits are nominally identical, the fitted x_{qp}^0 shows geometrical dependence, with x_{qp}^0 ratio ~ 2.5 between small pads (qubit A) and large pads (qubit B and C). We prove that this difference can be qualitatively explained below, with more details in the Supplementary Material.

We adopt a phenomenological energy-dependent diffusion model [33–35] to calculate the QP density arriving at the junction, assuming that the non-equilibrium QPs generated by high-energy radiation distribute uniformly in the qubit pads and elastically diffuse to the junction. The incoming QP energy is set to be near the gap energy of the system, and Neumann boundary conditions in the substrate-pad interface and junction are flux continuity. In the non-equilibrium regime, x_{qp}^0 in qubit A is about 2.7 times larger than the ones in qubits B and C due to the shorter distance that QPs travel in small pads to the junction. This value is close to the ratio obtained from experimental fitting. In the equilibrium regime, QPs are dominated by those that are thermally generated from the low-gap Al (instead of high-gap Nb). Since all qubits studied in this experiment share the same design of Al/AIO_x/Al Josephson junction, we expect the x_{qp}^{th} to be the same.

To quantify the contributions of QPs and TLSs to the variance of the qubit relaxation rate Γ_1 , we integrate the white noise and $1/f$ noise spectral densities over the measured frequency range at each temperature [see the fitted curves shown in Fig. 1(b)]. This allows us to separately determine the variances of the qubit depolarization rates induced by QPs, $\sigma_{qp}^2(\Gamma_1)$, and TLSs, $\sigma_{TLS}^2(\Gamma_1)$. The results are plotted as solid symbols in Fig. 3(a) and (b).

We first discuss the impact of QP fluctuations on the Γ_1 variance. From Fig. 3(a), we can see that $\sigma_{qp}^2(\Gamma_1)$ in all qubits exhibit a very similar trend: a weak temperature-dependence at $T < 100$ mK followed by a rapid increase at higher temperatures. It is also seen that in the low-temperature regime, qubit A is much more susceptible to the QP fluctuations, with $\sigma_{qp}^2(\Gamma_1)$ at least an order of magnitude higher than those observed for qubits B and C, while the latter two have similar Γ_1

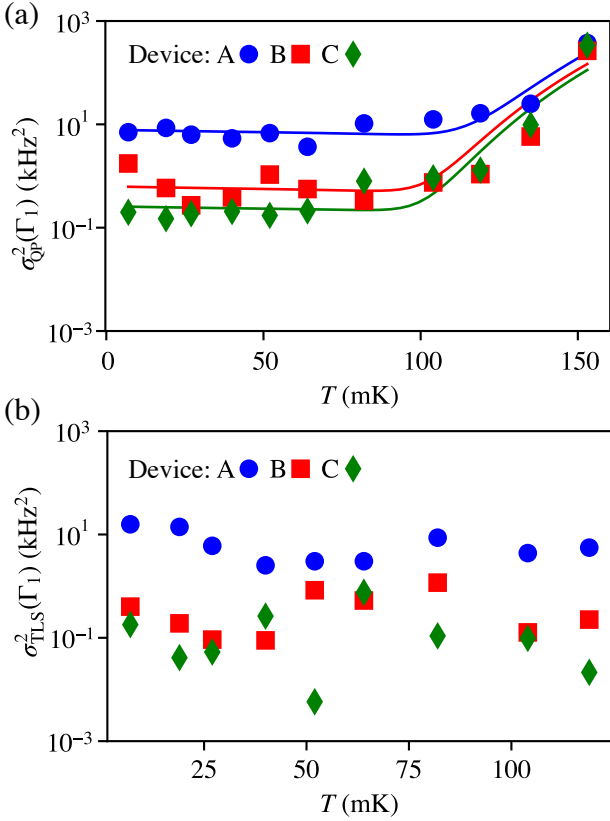


FIG. 3. Temperature dependence of qubit Γ_1 variance contributed by (a) QPs and (b) TLSs. In Figure (a), solid symbols represent the data extracted from experiments and solid lines are the fitting based on Eq. (2). The extracted fitting parameters are provided in Table I.

variances. With the model of QP diffusion and fluctuation, we can provide quantitative support in understanding these observations and further disentangle the impacts of non-equilibrium and thermal QPs on the qubit fluctuations. Assuming the number of QPs follows a Poisson distribution [18], we have the QP variance $\sigma^2(N_{\text{qp}})$ equals its mean value $\mu(N_{\text{qp}})$. Therefore, the variance $\sigma_{\text{qp}}^2(\Gamma_1)$ is given by:

$$\sigma_{\text{qp}}^2(\Gamma_1) = \eta^2(T) \left(\frac{x_{\text{qp}}^0}{n_{\text{cp}} V_{\text{eff}}^0} + \frac{x_{\text{qp}}^{\text{th}}}{n_{\text{cp}} V_{\text{eff}}^{\text{th}}} \right), \quad (2)$$

with $\eta(T) = \frac{16E_J}{\hbar\pi} \sqrt{\frac{E_C}{8E_J}} \sqrt{\frac{2\Delta}{\pi k_B T}} \exp\left(\frac{\hbar\omega_q}{2k_B T}\right) K_0\left(\frac{\hbar\omega_q}{2k_B T}\right)$. Here, the non-equilibrium and equilibrium QPs are assumed to be independent [28]. In Eq. (2), we define V_{eff}^0 and $V_{\text{eff}}^{\text{th}}$ as the effective volumes for non-equilibrium and thermal QPs, respectively, to reflect their distinct contributions to the fluctuations. Using previously obtained x_{qp}^0 , $x_{\text{qp}}^{\text{th}}$, and Δ [see Table I], we can fit the experimentally extracted $\sigma_{\text{qp}}^2(\Gamma_1)$ and obtain the values of V_{eff}^0 and $V_{\text{eff}}^{\text{th}}$ for each qubit. The fitted curves are shown as solid lines in Fig. 3(a), and the fitted V_{eff}^0 and $V_{\text{eff}}^{\text{th}}$ are also listed in Table I. In the non-equilibrium regime, the effective volume is expected to be proportional to $(v_F \cdot \tau_r)^3$, with the Fermi velocity v_F being the same for all

TABLE I. Fitting parameters extracted for three different transmon qubits. Here, x_{qp}^0 is the density of non-equilibrium QPs, Δ is the superconducting gap energy of Al, V_{eff}^0 and $V_{\text{eff}}^{\text{th}}$ are the effective volumes for non-equilibrium and thermal QPs, and Γ_{tls} is the depolarization rate from TLS.

Qubit	x_{qp}^0	$\Delta/2\pi$ (GHz)	V_{eff}^0 (μm^3)	$V_{\text{eff}}^{\text{th}}$ (μm^3)	Γ_{tls} (MHz)
A	1.4×10^{-7}	38.0	0.062	0.025	1.2×10^{-2}
B	5.5×10^{-8}	38.2	0.290	0.039	6.2×10^{-3}
C	5.5×10^{-8}	39.6	0.807	0.037	1.6×10^{-3}

qubits, and τ_r the QP recombination rate that is inversely proportional to x_{qp}^0 [18]. Therefore, we have $V_{\text{eff}}^0 \propto (1/x_{\text{qp}}^0)^3$. We notice that the ratio of V_{eff}^0 between device C (B) and A is about 13 (5) from the fitting. Indeed, this aligns with our data: the ratio of x_{qp}^0 between device A and C (B) is about 2.5 ($2.5^3 \sim 15$). Moreover, the difference in x_{qp}^0 can be supported by the diffusion process, from which the x_{qp}^0 ratio is calculated to be 2.7 between different pad sizes. In the thermal regime, the QP density dominated by the thermal generation in the Al junction leads increases significantly but does not substantially suppress the $V_{\text{eff}}^{\text{th}}$. On the other hand, $V_{\text{eff}}^{\text{th}}$ cannot exceed the upper limit set by the non-equilibrium QPs from the qubit pads when $k_B T$ approaches the Al gap energy. Therefore we approximate the $V_{\text{eff}}^{\text{th}}$ as a constant in Eq. (2). From the fit, we find the effective volume $V_{\text{eff}}^{\text{th}}$ for all the qubits approaches the same value, close to the volume of the Josephson junction $\sim 0.013 \mu\text{m}^3$. This is as expected since all qubits consist of the same Al junctions. Here we define the junction volume as the product of the junction area and the total thickness of Al layers.

In Fig. 3(b), we plot the $\sigma_{\text{TLS}}^2(\Gamma_1)$ induced by TLSs. Compared to the variance from QPs, the $\sigma_{\text{TLS}}^2(\Gamma_1)$ here show an overall weak dependence on temperature, with some local features. It is also observed that $\sigma_{\text{TLS}}^2(\Gamma_1)$ of qubit A is larger than qubit B and C, while the latter two show some consistency across the temperature range. We suggest that this can be qualitatively explained by TLS theory as well. The variance of qubit depolarization due to the interaction between a single TLS and an assemble of TLFs is given by [27]:

$$\sigma_{\text{tls}}^2(\Gamma_1) = A^4 \frac{16\gamma_2^2 \omega_\delta^2}{(\gamma_2^2 + \omega_\delta^2)^4} \left[\sum_i g_i^2 \left(1 - \tanh^2 \frac{\omega_{\text{ti}}}{2k_B T} \right) \right]^2, \quad (3)$$

where A denotes a constant related to the coupling strength and qubit matrix element, γ_2 describes the linewidth of the TLS, and g_i the coupling strength between the TLS and the i th TLF, with frequency ω_{ti} . When the temperature increases, the TLS linewidth gets larger, suppressing the amplitude of the Lorentzian, and thus the variance of the fluctuation. On the other hand, higher temperature leads to more frequent switching of the TLFs, increasing the last factor in Eq. (3). This discussion is based on a single TLS. In practice, multiple TLSs can couple simultaneously to the qubit, each with different dephasing rates and frequencies. As a result, the above two

competing factors for different TLSs may lead to the observed behavior in Fig. 3(b).

Our work underscores a practical need to stabilize qubit lifetimes. On one hand, theoretical proposals based on driving the qubits [36] or the TLSs [27] could provide ways to stabilize the fluctuations due to TLSs, without affecting the average lifetime. On the other hand, protocols for reducing fluctuations from QPs remain to be developed but may benefit from strategies to reduce QPs in general [32, 34, 37, 38].

In summary, we perform prolonged, statistical T_1 measurements on three superconducting transmon qubits across a broad temperature range. Different geometrical footprints and superconducting materials of these qubits enable us to disentangle the impacts of QPs and TLSs on the average and fluctuation of the qubit lifetime. The improvements in the average qubit lifetime can be explained by an optimization of the qubit design as well as a reduced loss of surface dielectric. More importantly, we find that the QP densities near the Josephson junction depend on the qubit footprints, *i.e.*, higher density in the small-footprint qubit. We further propose the concept of effective QP volume that scales cubically with the inverse of the non-equilibrium QP density, therefore providing quantitative support in understanding the discrepancy of the lifetime fluctuations in the qubits with different footprints. We suggest that these findings can provide a guideline for future optimization of qubit design and engineering.

This material is based upon work supported by the U.S. Department of Energy, Office of Science, National Quantum Information Science Research Centers, Superconducting Quantum Materials and Systems Center (SQMS) under contract number DE-AC02-07CH11359.

* szhu26@fnal.gov

- [1] J. Gambetta, IBM roadmap for scaling quantum technology, *IBM Res. Blog* (2020).
- [2] F. Arute, K. Arya, R. Babbush, D. Bacon, J. C. Bardin, R. Barends, R. Biswas, S. Boixo, F. G. Brandao, D. A. Buell, *et al.*, Quantum supremacy using a programmable superconducting processor, *Nature* **574**, 505 (2019).
- [3] A. Blais, A. L. Grimsmo, S. M. Girvin, and A. Wallraff, Circuit quantum electrodynamics, *Rev. Mod. Phys.* **93**, 025005 (2021).
- [4] Y. Y. Gao, M. A. Rol, S. Touzard, and C. Wang, Practical guide for building superconducting quantum devices, *PRX Quantum* **2**, 040202 (2021).
- [5] M. S. Alam, S. Belomestnykh, N. Bornman, G. Cencelo, Y.-C. Chao, M. Checchin, V. S. Dinh, A. Grassellino, E. J. Gustafson, R. Harnik, *et al.*, Quantum computing hardware for hep algorithms and sensing, [arXiv:2204.08605](https://arxiv.org/abs/2204.08605) (2022).
- [6] I. Siddiqi, Engineering high-coherence superconducting qubits, *Nat. Rev. Mater.* **6**, 875 (2021).
- [7] S. Krinner, S. Storz, P. Kurpiers, P. Magnard, J. Heinsoo, R. Keller, J. Luetolf, C. Eichler, and A. Wallraff, Engineering cryogenic setups for 100-qubit scale superconducting circuit systems, *EPJ Quantum Technol.* **6**, 2 (2019).
- [8] P. Krantz, M. Kjaergaard, F. Yan, T. P. Orlando, S. Gustavsson, and W. D. Oliver, A quantum engineer's guide to superconducting qubits, *Appl. Phys. Rev.* **6**, 021318 (2019).
- [9] C. Müller, J. Lisenfeld, A. Shnirman, and S. Poletto, Interacting two-level defects as sources of fluctuating high-frequency noise in superconducting circuits, *Phys. Rev. B* **92**, 035442 (2015).
- [10] P. Klimov, J. Kelly, Z. Chen, M. Neeley, A. Megrant, B. Burkett, R. Barends, K. Arya, B. Chiaro, Y. Chen, *et al.*, Fluctuations of energy-relaxation times in superconducting qubits, *Phys. Rev. Lett.* **121**, 090502 (2018).
- [11] S. Schlör, J. Lisenfeld, C. Müller, A. Bilmes, A. Schneider, D. P. Pappas, A. V. Ustinov, and M. Weides, Correlating decoherence in transmon qubits: Low frequency noise by single fluctuators, *Phys. Rev. Lett.* **123**, 190502 (2019).
- [12] M. Bal, A. A. Murthy, S. Zhu, F. Crisa, X. You, Z. Huang, T. Roy, J. Lee, D. van Zanten, R. Pilipenko, *et al.*, Systematic improvements in transmon qubit coherence enabled by niobium surface encapsulation, *npj Quantum Inf.* **10**, 43 (2024).
- [13] M. Carroll, S. Rosenblatt, P. Jurcevic, I. Lauer, and A. Kandala, Dynamics of superconducting qubit relaxation times, *npj Quantum Inf.* **8**, 132 (2022).
- [14] C. Müller, J. H. Cole, and J. Lisenfeld, Towards understanding two-level-systems in amorphous solids: insights from quantum circuits, *Rep. Prog. Phys.* **82**, 124501 (2019).
- [15] C. Wang, C. Axline, Y. Y. Gao, T. Brecht, Y. Chu, L. Frunzio, M. Devoret, and R. J. Schoelkopf, Surface participation and dielectric loss in superconducting qubits, *Appl. Phys. Lett.* **107** (2015).
- [16] J. Gao, M. Daal, A. Vayonakis, S. Kumar, J. Zmuidzinas, B. Sadoulet, B. A. Mazin, P. K. Day, and H. G. Leduc, Experimental evidence for a surface distribution of two-level systems in superconducting lithographed microwave resonators, *Appl. Phys. Lett.* **92** (2008).
- [17] J. J. Burnett, A. Bengtsson, M. Scigliuzzo, D. Niepce, M. Kudra, P. Delsing, and J. Bylander, Decoherence benchmarking of superconducting qubits, *npj Quantum Inf.* **5**, 54 (2019).
- [18] P. J. de Visser, J. J. A. Baselmans, P. Diener, S. J. C. Yates, A. Endo, and T. M. Klapwijk, Number fluctuations of sparse quasiparticles in a superconductor, *Phys. Rev. Lett.* **106**, 167004 (2011).
- [19] S. Simbierowicz, C. Shi, M. Collodo, M. Kirste, F. Hassani, J. M. Fink, J. Bylander, D. Perez Lozano, and R. Lake, Qubit energy-relaxation statistics in the bluefors quantum measurement system, *Bluefors Oy*, **8** (2021).
- [20] K. Li, S. Dutta, Z. Steffen, B. Palmer, C. Lobb, and F. Wellstood, Power-law scaling of relaxation time fluctuations in transmon qubits, *IEEE Trans. Appl. Supercond.* **33**, 1 (2023).
- [21] F. Yan, S. Gustavsson, A. Kamal, J. Birenbaum, A. P. Sears, D. Hover, T. J. Gudmundsen, D. Rosenberg, G. Samach, S. Weber, *et al.*, The flux qubit revisited to enhance coherence and reproducibility, *Nat. Commun.* **7**, 12964 (2016).
- [22] A. Romanenko, R. Pilipenko, S. Zorzetti, D. Frolov, M. Awida, S. Belomestnykh, S. Posen, and A. Grassellino, Three-dimensional superconducting resonators at t_j 20 mk with photon lifetimes up to $\tau = 2$ s, *Phys. Rev. Appl.* **13**, 034032 (2020).
- [23] S. Zhu, F. Crisa, M. Bal, A. Murthy, J. Lee, Z. Sung, A. Lunin, D. Frolov, R. Pilipenko, D. Bafia, *et al.*, High quality superconducting Nb co-planar resonators on sapphire substrate, [arXiv:2207.13024](https://arxiv.org/abs/2207.13024) (2022).
- [24] K. D. Crowley, R. A. McLellan, A. Dutta, N. Shumiya, A. P. Place, X. H. Le, Y. Gang, T. Madhavan, M. P. Bland, R. Chang, *et al.*, Disentangling losses in tantalum superconducting circuits, *Phys. Rev. X* **13**, 041005 (2023).
- [25] C. M. Wilson, L. Frunzio, and D. E. Prober, Time-resolved measurements of thermodynamic fluctuations of the particle number in a nondegenerate fermi gas, *Phys. Rev. Lett.* **87**, 067004 (2001).

- (2001).
- [26] X. You, A. A. Clerk, and J. Koch, Positive- and negative-frequency noise from an ensemble of two-level fluctuators, *Phys. Rev. Research* **3**, 013045 (2021).
 - [27] X. You, Z. Huang, U. Alyanak, A. Romanenko, A. Grassellino, and S. Zhu, Stabilizing and Improving Qubit Coherence by Engineering the Noise Spectrum of Two-Level Systems, *Phys. Rev. Applied* **18**, 044026 (2022).
 - [28] K. Serniak, M. Hays, G. De Lange, S. Diamond, S. Shankar, L. Burkhardt, L. Frunzio, M. Houzet, and M. Devoret, Hot nonequilibrium quasiparticles in transmon qubits, *Phys. Rev. Lett.* **121**, 157701 (2018).
 - [29] L. I. Glazman and G. Catelani, Bogoliubov quasiparticles in superconducting qubits, *SciPost Phys. Lect. Notes* , 31 (2021).
 - [30] In the fitting, we assume the x_{qp}^0 to be the same for devices B and C, as they share the same pad and junction design.
 - [31] T. Connolly, P. D. Kurilovich, S. Diamond, H. Nho, C. G. Böttcher, L. I. Glazman, V. Fatemi, and M. H. Devoret, Coexistence of nonequilibrium density and equilibrium energy distribution of quasiparticles in a superconducting qubit, *Phys. Rev. Lett.* **132**, 217001 (2024).
 - [32] P. Kamenov, T. DiNapoli, M. Gershenson, and S. Chakram, Suppression of quasiparticle poisoning in transmon qubits by gap engineering, [arXiv:2309.02655](https://arxiv.org/abs/2309.02655) (2023).
 - [33] R.-P. Riwar and G. Catelani, Efficient quasiparticle traps with low dissipation through gap engineering, *Phys. Rev. B* **100**, 144514 (2019).
 - [34] J. M. Martinis, Saving superconducting quantum processors from decay and correlated errors generated by gamma and cosmic rays, *npj Quantum Inf.* **7**, 90 (2021).
 - [35] U. Alyanak, Z. Huang, W.-T. Lin, X. You, A. Romanenko, A. Grassellino, Y.-K. Kim, and S. Zhu, Modeling and testing novel quasiparticle traps on superconducting qubits via geometric gap engineering, *Bull. Am. Phys. Soc.* (2024).
 - [36] S. Matityahu, A. Shnirman, and M. Schechter, Stabilization of Qubit Relaxation Rates by Frequency Modulation, *Phys. Rev. Applied* **16**, 044036 (2021).
 - [37] V. Iaia, J. Ku, A. Ballard, C. Larson, E. Yelton, C. Liu, S. Patel, R. McDermott, and B. Plourde, Phonon downconversion to suppress correlated errors in superconducting qubits, *Nat. Commun.* **13**, 6425 (2022).
 - [38] R.-P. Riwar, A. Hosseinkhani, L. D. Burkhardt, Y. Y. Gao, R. J. Schoelkopf, L. I. Glazman, and G. Catelani, Normal-metal quasiparticle traps for superconducting qubits, *Phys. Rev. B* **94**, 104516 (2016).

Supplementary Material for “Disentangling the Impact of Quasiparticles and Two-Level Systems on the Statistics of Superconducting Qubit Lifetime”

Shaojiang Zhu,¹ Xinyuan You,¹ Ugur Alyanak,^{1,2} Mustafa Bal,¹ Francesco Crisa,¹
Sabrina Garattoni,¹ Andrei Lunin,¹ Roman Pilipenko,¹ Akshay Murthy,¹ Alexander Romanenko,¹ and Anna Grassellino¹

¹*Superconducting Quantum Materials and Systems Center,
Fermi National Accelerator Laboratory, Batavia, IL 60510, USA*
²*Department of Physics, University of Chicago, Chicago, IL 60637, USA*

QUBIT LAYOUT

The eight fixed-frequency transmon qubits on each Sapphire chip with $7.5 \times 7.5 \text{ mm}^2$ size are grouped into three different geometrical footprints, which are expected to have different surface participation ratios. Each qubit is capacitively coupled to an independent $\lambda/4$ CPW resonator, then the resonator is inductively coupled to a common feedline where the microwave signal is transmitted. Figure 1 shows the qubit chip layout. With the same qubit layout design, we perform a systematical study on the qubit lifetime T_1 by encapsulating different materials on top of the same Nb base layer while keeping all fabrication processes, Josephson junctions, and measurement configurations and methods nominally identical [1]. The three qubits under discussion in this work are labeled as A, B, and C on the layout too. All qubits are designed to operate around 4 GHz, and the resonances of readout resonators are between 7-8 GHz.

ENERGY PARTICIPATION RATIO SIMULATION

We perform the energy participation ratio (EPR) simulation with a 3D microwave model, which is necessary for the qubit layout due to its irregular geometries compared with the CPW resonator [2, 3].

Due to the extraordinary geometrical aspect ratio of the qubit pads dimensions (hundreds of micro-meters) to the thickness of the thin dielectric layer (a few nano-meters) on the surface of the metal pads, careful considerations of the tradeoff between simulation accuracy and cost is necessary. Different from the other strategies in the full 3D qubit simulations [4, 5], we first adopt thick (200 nm) dielectric to perform the simulation with high meshing size, then we gradually reduce the dielectric thickness without sacrificing the simulation accuracy (meshing size) to get the EPR values at different dielectric thicknesses down to 20 nm. We find a good linear relationship between EPR and dielectric thickness, therefore we can obtain the EPR at 5 nm by extrapolating the simulated data (see Fig. 2). During the simulation, we also carefully consider the real profiles of the etched film, such as a certain degree of the film sidewall slope, the rounded edge corner, and the very shallow trenches on the Sapphire substrate due to over-etching. Based on the material characterizations, we only consider the metal-air interface in the simulation, using the measured dielectric thickness of 5 nm with dielectric constant $\epsilon = 10$ [2–4].

We find that the EPR of qubit A is about two times larger than that of qubit B. We also find that, for qubit C, the EPR of the surface (TaO_x) and the sidewall (NbO_x) are the same, so the effective dielectric loss combining both materials is about 5.5 times smaller than the loss of NbO_x . This can qualitatively explain the ~ 4 times improvement of TLS loss from qubit B to C in the experiments.

TEMPERATURE DEPENDENCE OF QUBIT LIFETIME INDUCED BY TWO-LEVEL SYSTEMS

In our analysis of qubit lifetime as a function of temperature, we assume the contribution from two-level systems (TLSs) to be independent of temperature. Below, we present the derivation supporting this assumption.

According to the standard TLS model [6], the noise spectral density, $S_{\text{TLS}}(\omega)$, of a single TLS is described by:

$$S_{\text{TLS}}(\omega) = \frac{1 + \langle \sigma_z \rangle_{\text{eq}}}{2} \frac{2\gamma_2}{(\omega - \omega_0)^2 + \gamma_2^2} + \frac{1 - \langle \sigma_z \rangle_{\text{eq}}}{2} \frac{2\gamma_2}{(\omega + \omega_0)^2 + \gamma_2^2}, \quad (1)$$

where $\langle \sigma_z \rangle_{\text{eq}} = \tanh\left(\frac{\omega_0}{2k_B T}\right)$ represents the equilibrium polarization, dependent on temperature T , γ_2 is the TLS dephasing rate, and ω_0 is the resonance frequency of the TLS. When a qubit is coupled to the TLS, the first term corresponds to a Lorentzian centered at positive frequency ω_0 and primarily contributes to qubit relaxation, whereas the second term, centered at negative frequency $-\omega_0$, predominantly results in qubit excitation. The same temperature dependence gives rise to the phenomenon that

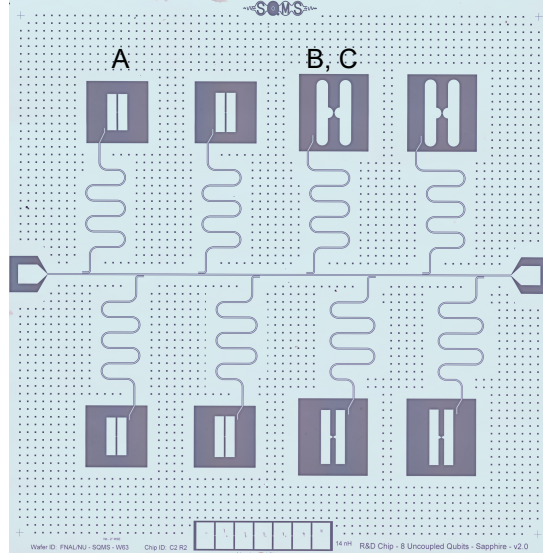


FIG. 1. Microscope image of the qubit chip, showing all eight isolated qubits with each own $\lambda/4$ CPW resonator that inductively coupled to the common feedline. The capacitor pad size of qubit A is $120 \times 510 \mu\text{m}^2$ with $20 \mu\text{m}$ gap, and the one of qubit B and C are $150 \times 720 \mu\text{m}^2$ with $150 \mu\text{m}$ gap.

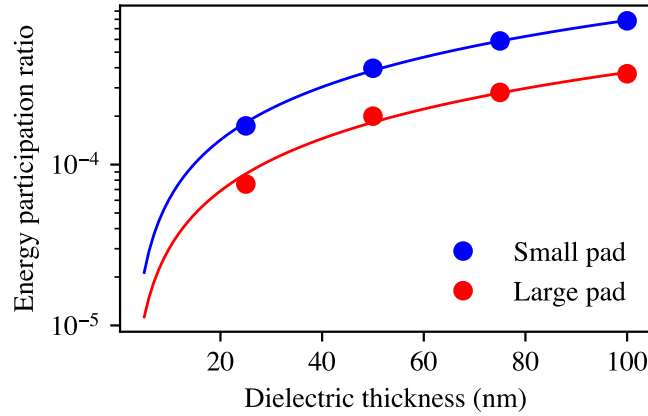


FIG. 2. Simulated EPR for small pad (blue dot) and large pad (red dot). Solid curves are the linear fit of each data set, from which we can extrapolate the EPR at the thickness of 5 nm for both pad sizes. The EPR ratio of the two pads at 5 nm is about 2.

TLSs can be saturated with high temperature to increase the resonator Q , which is inversely proportional to the difference of the excitation and relaxation process, *i.e.*, $\langle \sigma_z \rangle_{\text{eq}}$. However, in the context of qubit lifetime, the previous statement is no longer true. Contrary to being dictated by the difference between the relaxation and excitation processes, the qubit's depolarization rate (inverse of lifetime) is governed by their summation. Therefore, the dependence on $\langle \sigma_z \rangle_{\text{eq}}$ is suppressed (by considering a qubit is in close resonance with the TLS). While the TLS dephasing rate γ_2 may exhibit a modest temperature dependence, an ensemble of TLSs with a specific distribution renders the averaged spectral density effectively temperature-independent [7].

QUASIPARTICLE DENSITY CALCULATION

To calculate the ratio of x_{qp}^0 that reach the junction for different geometries, we use a 1D phenomenological diffusion model [8, 9] that assumes Neumann boundary conditions in the pad-substrate interface and the Josephson Junction, this choice makes sure the current will be continuous in both during phonon mediated quasiparticle creation at the substrate and quasiparticle

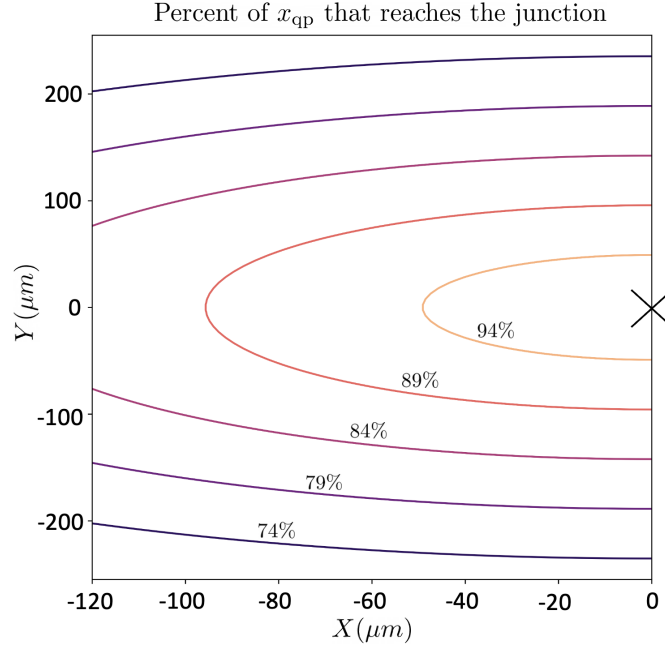


FIG. 3. Percent of non-equilibrium quasiparticle density x_{qp}^0 that reaches the junction given incoming position (X, Y) calculated for the small pad geometry (qubit A), where the junction lies at $(0, 0)$ indicated with a cross.

tunneling across the junction. We use the following diffusion equation,

$$\frac{\partial \rho_\epsilon(x, t)}{\partial t} = D(\epsilon, x) \frac{\partial^2 \rho_\epsilon(x, t)}{\partial x^2} - \frac{\rho_\epsilon(x, t)}{\tau(\epsilon, x)} + j(\epsilon, x, t), \quad (2)$$

where $\rho_\epsilon(x, t)$ is the spatio-temporal quasiparticle density, τ is the QP lifetime, and D is the diffusion coefficient. In this 1D model, we set the length of the system to be L , the distance between the substrate-pad interface to the junction. The incoming quasiparticle energy is assumed to be around Δ , and $j(\epsilon, x, t)$ is the injection term non-zero only for $t = 0$ and a small neighborhood of $x = 0$. With this information, we can set up a relationship between x_{qp}^0 and $\rho_\epsilon(x, t)$, *i.e.*,

$$x_{qp}^0 \equiv \int_0^{t_{\max}} dt' \rho_{(\epsilon \approx \Delta)}(L, t'), \quad (3)$$

where t_{\max} is set to be much longer than the expected quasi-particle time of flight from the pad to the junction, and shorter than the time the system takes to generate another quasiparticle bunch due to external sources. Since the measurable quantity that affects T_1 and its fluctuations is the density that tunnels across the junction, and incoming energy is near Δ , we set $x = L$ and $\epsilon = \Delta$.

The remaining step is to convert our 3D junction geometry to a 1D length. Instead of finding the mean distance between the pad and junction, we calculate the percentage of density reached to the junction using our 1D model for all possible paths the quasiparticle can take across the pad geometry, and average these percentages for the different pad geometries A, B and C (see Fig. 3 for percentages of qubit A). The results show that assuming the incoming quasiparticle densities are the same for all pads, there is a factor of 2.73 difference in x_{qp}^0 between pad A and pads B and C.

-
- [1] M. Bal, A. A. Murthy, S. Zhu, F. Crisa, X. You, Z. Huang, T. Roy, J. Lee, D. van Zanten, R. Pilipenko, *et al.*, Systematic improvements in transmon qubit coherence enabled by niobium surface encapsulation, [npj Quantum Inf. **10**, 43 \(2024\)](#).
 - [2] J. Wenner, R. Barends, R. Bialczak, Y. Chen, J. Kelly, E. Lucero, M. Mariantoni, A. Megrant, P. O'Malley, D. Sank, *et al.*, Surface loss simulations of superconducting coplanar waveguide resonators, [Appl. Phys. Lett. **99** \(2011\)](#).
 - [3] W. Woods, G. Calusine, A. Melville, A. Sevi, E. Golden, D. K. Kim, D. Rosenberg, J. L. Yoder, and W. D. Oliver, Determining interface dielectric losses in superconducting coplanar-waveguide resonators, [Phys. Rev. Appl. **12**, 014012 \(2019\)](#).
 - [4] C. Wang, C. Axline, Y. Y. Gao, T. Brecht, Y. Chu, L. Frunzio, M. Devoret, and R. J. Schoelkopf, Surface participation and dielectric loss in superconducting qubits, [Appl. Phys. Lett. **107** \(2015\)](#).

- [5] J. M. Gambetta, C. E. Murray, Y.-K.-K. Fung, D. T. McClure, O. Dial, W. Shanks, J. W. Sleight, and M. Steffen, Investigating surface loss effects in superconducting transmon qubits, [IEEE Trans. Appl. Supercond.](#) **27**, 1 (2016).
- [6] C. Müller, J. H. Cole, and J. Lisenfeld, Towards understanding two-level-systems in amorphous solids: insights from quantum circuits, [Rep. Prog. Phys.](#) **82**, 124501 (2019).
- [7] X. You, A. A. Clerk, and J. Koch, Positive- and negative-frequency noise from an ensemble of two-level fluctuators, [Phys. Rev. Research](#) **3**, 013045 (2021).
- [8] R.-P. Riwar and G. Catelani, Efficient quasiparticle traps with low dissipation through gap engineering, [Phys. Rev. B](#) **100**, 144514 (2019).
- [9] J. M. Martinis, Saving superconducting quantum processors from decay and correlated errors generated by gamma and cosmic rays, [npj Quantum Inf.](#) **7**, 90 (2021).